

Electronic Supplementary Information

Descriptor-Driven Design of Carbon Nitride for Visible Light Photocatalysis

Xuying Li,^a Haoxin Mai,^{a*} Tsuyoshi Takata,^b Nicholas Cox,^c Qi Li,^a Junlin Lu,^a Xiaoming Wen,^a Edwin L. H. Mayes,^d Salvy P. Russo,^e Takashi Hisatomi,^{b†} Kazunari Domen,^{b†g} Dehong Chen,^{a†*} and Rachel A. Caruso^{a*}

a. Applied Chemistry and Environmental Science, School of Science, STEM College, RMIT University, Melbourne, Victoria 3000, Australia; Email: rachel.caruso@rmit.edu.au; dhchen@qust.edu.cn; haoxin.mai@rmit.edu.au.

b. Research Initiative for Supra-Materials, Shinshu University, Nagano, Japan.

c. Research School of Chemistry, The Australian National University, Canberra, ACT 2601, Australia.

d. RMIT Microscopy and Microanalysis Facility, STEM College, RMIT University, Melbourne, Victoria 3001, Australia

e. ARC Centre of Excellence in Exciton Science, School of Science, RMIT University, Melbourne, Victoria 3000, Australia

f. Institute for Aqua Regeneration, Shinshu University, Nagano, Japan.

g. Office of University Professors, The University of Tokyo, Tokyo, Japan.

† Current address: College of Materials Science and Engineering, Qingdao University of Science and Technology.

Materials and Methods

1. Chemicals

Melamine (99%), citric acid monohydrate (CA, ACS reagent, $\geq 99\%$), lithium hydroxide monohydrate (LiOH, ACS reagent, $\geq 98\%$), potassium iodide (KI, $\geq 95\%$), hydrochloric acid (HCl, 32%), ammonium molybdate tetrahydrate ($\text{H}_{24}\text{Mo}_7\text{N}_6\text{O}_{24}\cdot 4\text{H}_2\text{O}$, $\geq 99\%$), methanol (ACS reagent), 5,5-dimethyl-1-pyrroline N-oxide (DMPO) and p-benzoquinone (p-BQ, reagent grade, $\geq 98\%$) were purchased from Sigma-Aldrich. Hydrogen peroxide (H_2O_2 , 30%) and silver nitrate (AgNO_3) were purchased from Rowe Scientific. $\text{Na}_2\text{PtCl}_6\cdot 6\text{H}_2\text{O}$ (99.9%) was purchased from Wako Pure Chemical Industries. All reagents were used as received. Milli-Q water was collected from a Milli-Q IQ 7000 system with resistivity higher than $18.2 \text{ M}\Omega\cdot\text{cm}$.

2. Synthesis of CN samples

2.1. Synthesis of solvothermally treated melem supramolecular precursors

The preparation of the precursor was carried out following our previous report with some modifications incorporated.¹ Raw melem was prepared by calcining melamine in a crucible covered by a lid in a muffle furnace at $420 \text{ }^\circ\text{C}$ for 4 h under air with a ramp rate of $4 \text{ }^\circ\text{C min}^{-1}$. The obtained powder was used as the precursor for the following experiments without further treatment.

For the synthesis of the self-assembled melem precursor of cyano-introduced C-doped CN (CCN-Cy), 0.50 g CA was first dissolved in 60 mL Milli-Q water. Then 1.00 g melem was added into the CA solution and stirred for 30 min, followed by continuous sonication in an ultrasonic bath for 20 min. After sonication, 20 mL ethanol was added to the mixture, and it was stirred for another 30 min. Subsequently, 1.6 mL of aqueous 5 M LiOH was added to the solution followed by stirring for 30 min. The melem suspension was then transferred to a 100 mL Teflon-lined autoclave and heated at $200 \text{ }^\circ\text{C}$ for 16 h. The product was collected by filtration and washed with 1 M HCl solution and Milli-Q water three times to remove the residue alkali ions. The 4cyano-introduced C-doped CN (CCN-4Cy) precursor was prepared using 2 mL of 5 M LiOH, keeping all other conditions the same with cyano-introduced C-doped CN.

For the synthesis of the C-doped CN precursor (CCN), the process is identical to the preparation of the precursor for cyano-incorporated C-doped CN, except that no LiOH was added to the precursor solution. Similarly, 2C-doped CN (2CCN) and 4C-doped CN (4CCN) precursors were prepared by adding 1.00 g

and 2.00 g of CA to the precursor solution, respectively, while keeping all other conditions the same as for the C-doped CN precursor.

For reference, the precursor of bulk CN (BCN) was synthesized by the same conditions as the above two precursors, without the addition of CA or an alkaline substance.

In addition, melem hydrate was prepared for reference by treating melem using the solvothermal method under the same conditions, without the addition of CA or an alkaline substance and a solvothermal time of 8 h.

2.2. Synthesis of BCN and defect-engineered CN samples

The BCN, CCN, 2CCN, 4CCN, CCN-Cy and CCN-4Cy were obtained by calcining their as prepared precursors in a crucible covered with a lid at 500 °C for 2 h (ramp rate of 10 °C min⁻¹) in a muffle furnace in air.

3. Materials characterization

The morphology of the samples were viewed using a NOVA scanning electron microscope (SEM) operating at 3 kV with a 5 nm iridium coating of the samples. The crystal structure was measured on a Bruker D4 X-ray diffractometer (XRD) with Cu K α . Thermogravimetric analysis (TGA) was carried out on a Perkin Elmer STA6000 Thermogravimetric Analyser heating from 30 to 850 °C at a ramp of 10 °C min⁻¹ under air flow (20 mL min⁻¹). High-angle annular dark-field scanning transmission electron microscopy (HAADF-STEM) and energy dispersive spectroscopy (EDS) were conducted on a JEOL JEM-F200 TEM operating at 200 kV. The inductively coupled plasma-mass spectrometer (ICP-MS) was an Agilent 7700 series ICP-MS. The elemental analysis was conducted using Thermo Scientific K-Alpha X-ray photoelectron spectroscopy (XPS) with an Al K α radiation source, which emitted photon energy of 1486.6 eV. The chemical bond information was analysed by Perkin Elmer Fourier transform infrared (FT-IR) spectroscopy with a diffuse reflectance accessory in the range of 400-4000 cm⁻¹. The diffuse reflectance spectroscopy, DRS, UV-vis spectra were measured on a UV-vis spectrometer (Cary 5000, Agilent) equipped with a praying mantis accessory using BaSO₄ as the reference. The Brunauer-Emmett-Teller (BET) surface area and Barrett-Joyner-Halenda (BJH) pore volume of the samples were collected by a Micromeritics Tristar II surface area and porosity analyser using N₂ as the adsorbate. Prior to measurement, samples were degassed at 120 °C for at least 8 h on a vacuum line. Specific surface areas were calculated by BET theory using adsorption values in the range P/P₀ = 0.05-0.20. The pore volume and pore size distribution were determined using the BJH model applied to the adsorption data, and the total pore volume

was estimated from the adsorbed amount at $P/P_0 = 0.983$. The time-resolved photoluminescence (TRPL) was obtained using a time-correlated single photon counting technique under the excitation of a 375 nm laser (pulse duration 40 ps, repetition rate 5 MHz). All the decay curves were fitted to a tri-exponential function of time (t), using the equation as follows: $F(t) = \sum A_i \exp(-t/\tau_i)$, where i represents the i^{th} component of a given multiexponential decay process, τ_i represents the values of the lifetime components and A_i represents the corresponding amplitudes. The effective decay times were calculated by the equation: $\tau_{\text{eff}} = \sum A_i \tau_i / \sum A_i$. CW X-band solution-phase electron paramagnetic resonance (EPR) spectra were collected on a 9.8 GHz X-band Bruker Elexsys E580 spectrometer with an ER 4103TM resonator at room temperature to detect reactive oxidation radicals generated in photocatalysis. Reported spectra were recorded with a field modulation of 0.05 mT and a microwave power of 100 mW. All samples were measured in a quartz flat cell with DMPO as a trapping agent. The measurements were conducted *in situ*, e.g., the sample was illuminated inside the EPR cavity with a 250 W Oriel Xenon lamp equipped with a 420 nm cut-off filter.

4. Photocatalytic testing

The photocatalytic activity of the sample was investigated by hydrogen production and the degradation of tetracycline hydrochloride (TC-HCl) under visible light irradiation.

In the hydrogen production, 10 mL methanol was used as the sacrificial reagent and mixed with 90 mL distilled water containing an optimized amount of photocatalyst sample (10 mg). 2 wt.% of Pt co-catalyst was loaded on the CN samples by photodeposition. Specifically, 2.5 mg of $\text{Na}_2\text{PtCl}_6 \cdot 6\text{H}_2\text{O}$ was dissolved in 25 mL of Milli-Q H_2O . Then 10 mg of photocatalyst was added to 5.75 mL of this solution. The mixture was stirred under irradiation by a 300 W xenon lamp (LX-300F, INOTEX CO., LTD.) for 30 min, during which $\text{Na}_2\text{PtCl}_6 \cdot 6\text{H}_2\text{O}$ was reduced to metallic Pt by photoexcited electrons from the photocatalyst. The hydrogen evolution reactions were conducted in a Pyrex top-irradiated reaction vessel connected to a glass-closed gas circulation system. Argon gas was introduced into the circulation system as a carrier gas after removing the air. The total background pressure of argon and water vapor was ~ 7 kPa. The temperature of the reactant solution was maintained at 288 K using cooling water. The reactions were performed under irradiation from a 300 W xenon lamp (LX-300F, INOTEX CO., LTD.) equipped with a cutoff filter ($\lambda > 420$ nm). The amounts of gas produced were measured by gas chromatography (Shimadzu GC-8A with a thermal conductivity detector, MS-5A columns and argon carrier gas). The reaction rates were determined from a linear regression fit once hydrogen evolution became mostly stable.

In the H₂O₂ generation, the visible light source was a 500 W Xe lamp equipped with a 420 nm cut-off filter, placed 15 cm beyond the reactor (light intensity of 1769 W·m⁻²). The reaction solution temperature was maintained at 20 °C by a circulating water bath. For photocatalytic experiments, 10 mg of the photocatalyst was added to 50 mL 10 vol.% ethanol solution with no change in the solution pH and stirred in the dark for 1 h to reach sorption equilibrium prior to light irradiation. Compressed air (50 mL·min⁻¹, BOC air 055) was continuously bubbled through the reaction solution. During the 2 h of light irradiation, 1.5 mL of reaction suspension was collected at 30 min intervals. The concentration of H₂O₂ was monitored by iodometric titration. Specifically, reaction solution was centrifuged at 9000 rpm for 15 min, then 1 mL of supernatant was mixed with 0.5 mL KI (0.1 M) and 0.5 mL ammonium molybdate tetrahydrate (0.1 mM) and allowed to stabilize for 5 min. Finally, the absorbance of the coloured solution was detected from the characteristic peak at 350 on a Cary 500 UV-Vis-NIR spectrometer.

The radical trapping tests were conducted under identical conditions as the photodegradation experiments, where 1 mL 10 mM of p-BQ or AgNO₃ were added as the superoxide radical or photogenerated electron scavenger, respectively.

5. Density Functional Theory (DFT) Calculations

Geometrical optimizations and electronic structure calculations were performed using the DFT^{2, 3} as implemented with Vienna Ab initio Simulation Package (VASP) code^{4, 5} on the basis of the plane-wave method. The Perdew-Burke-Ernzerhof (PBE)⁶ functional for the generalized gradient approximation was used to describe the exchange-correlation potential. The Projector-Augmented-Wave (PAW)^{7, 8} method was used to describe the interaction between the ionic core and valence electrons.

The structures of C₂₄N₃₆H₁₂ (BCN), C₂₈N₃₂H₁₂ (C-doped CN, CCN), C₃₀N₃₀H₁₂ (2C-doped CN, 2CCN), C₃₂N₂₈H₁₂ (4C-doped CN, 4CCN), C₂₈N₃₂H₁₂-cyano (cyano-introduced C-doped CN, CCN-Cy) and C₂₈N₃₂H₁₂-4cyano (4cyano-introduced C-doped, CCN-4Cy) were constructed based on structure characterization (e.g., XRD, FTIR) and our previous result.¹ In all the structural models, the spheres coloured white, blue, and grey represent atoms of H, N, and C, respectively. Based on the convergence tests, a plane-wave cut-off energy of 500 eV was selected, and the Γ -centred k-points mesh of 12×12×1 was employed for sampling the Brillouin zones. The atomic positions were fully relaxed until the force on each atom was smaller than 0.01 eV/Å and the convergence threshold for the self-consistent field was 10⁻⁵ eV. To calculate band structure, the selected k-path was Γ (0, 0, 0) – X (0.5, 0, 0) – S (0.5, 0.5, 0) – Y (0,

0.5, 0) – Γ (0, 0, 0) – S (0.5, 0.5, 0).⁹ The typical structures (most stable configurations) of the CN samples are shown in **Fig. S1a-f**.

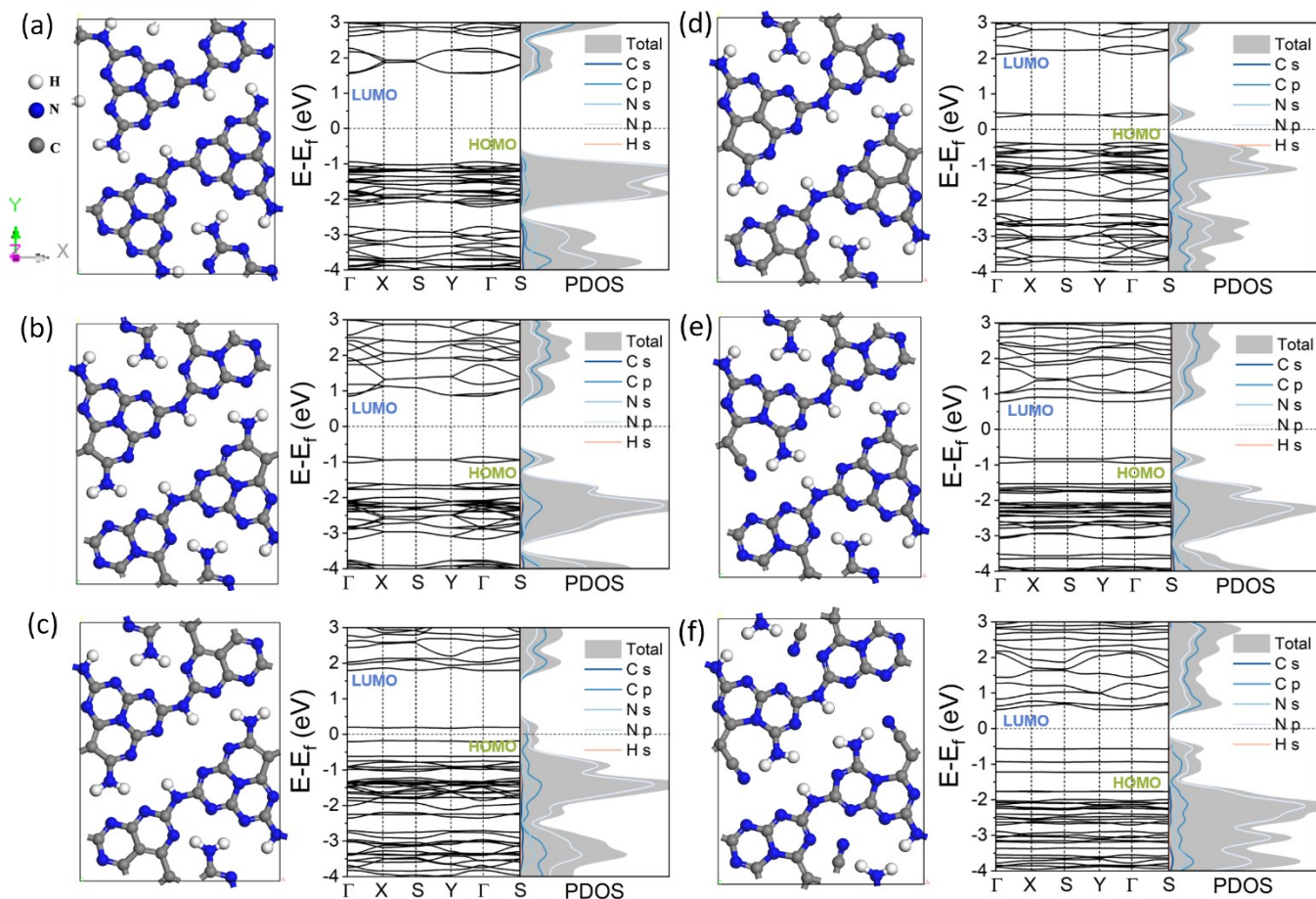


Fig. S1. Left to right: Structure models, calculated band structure, and corresponding partial density of states (PDOS) for (a) $C_{24}N_{36}H_{12}$ (BCN), (b) $C_{28}N_{32}H_{12}$ (CCN), (c) $C_{30}N_{30}H_{12}$ (2CCN), (d) $C_{32}N_{28}H_{12}$ (4CCN), (e) $C_{28}N_{32}H_{12}$ -cyano (CCN-Cy), and (f) $C_{28}N_{32}H_{12}$ -4cyano (CCN-4Cy). Adapted from ¹.
Copyright 2024, Royal Society of Chemistry.

To calculate the electron density distribution in the excited state, the geometrical optimization of the configurations was performed by manually setting the frontier states electronic occupation for each k-point through the VASP tags FERWE and FERDO.

The effective mass of the charge carriers could be found from equation (S1) based on the energy band structure:

$$E(k) = E_0 + \frac{\hbar^2 k^2}{2m} \quad (\text{S1})$$

where m is effective mass of the charge carriers, k is the wave vector, E_0 is the energy of the band edge, \hbar is the reduced Plank constant and $E(k)$ is the energy of an electron or a hole at wave vector k in that band. As a result, m could be obtained by equation (S2):¹⁰

$$m = \hbar^2 \times \left(\frac{\partial^2 E}{\partial k^2} \right)^{-1} \quad (\text{S2})$$

The effective mass of an electron (m_e) and hole (m_h), therefore, could be determined via parabolic fitting of the bands around the conduction band minimum (CBM) and valence band maximum (VBM) and

calculating their $\frac{\partial^2 E}{\partial k^2}$, respectively.¹¹

Both the d-band centre of Pt and p-band centres of C and N were calculated by taking the weighted mean energy of the projected density of states of Pt-d and C,N-p states (both occupied and unoccupied states) relative to the Fermi level.

The adsorption energy (E_{ad}) of H₂O, O₂, and H* was calculated as follows:

$$E_{ad} = E_{sub+adsorbate} - E_{sub} - E_{adsorbate} \quad (\text{S3})$$

where $E_{sub+adsorbate}$, E_{sub} , and $E_{adsorbate}$ were the total energy of the adsorbate molecule (H₂O, O₂ or H*) on the CN samples, the total energy of the CN samples, and the total energy of the adsorbate molecule (H₂O, O₂ or 1/2 H₂), respectively. The stable adsorption configurations for the H₂O molecule and H* on the CN samples are shown in **Fig. S3** and **Fig. S4**.

The free energy (ΔG) of H₂O, O₂, hydrogen, as well as the intermediates (*OOH, HOOH*) on the surface of CN samples was calculated as:

$$\Delta G = E_{ad} + \Delta E(ZPE) - T\Delta S \quad (\text{S4})$$

where $\Delta E(ZPE)$ is the zero-point energy change and ΔS is the entropy change. $\Delta E(ZPE) - T\Delta S$ is estimated to be 0.24 eV at 298 K according to the literature.¹²

To simulate the structure of the CN samples with Pt nanocluster co-catalysts, one Pt atom is added onto the CN samples after geometrical optimization. To simplify the calculation, we only consider the case where there is one Pt atom on the catalysts.¹³⁻¹⁵ The GGA+U approach was applied to describe the strong correlations of Pt d-manifolds. Three Hubbard-U values (2.5, 3.0, 4.5) were tested,¹⁶ and we found that although adding the U value would lead to a smaller total energy of the CN-Pt, CN-Pt-H₂O, and CN-Pt-H* systems, it would not change the most stable structure of the CN-Pt samples, neither would the U value

change the calculation results of the H₂O adsorption energy and the H* adsorption energy. Therefore, to simplify the calculation, in the following calculation we did not take the U value into account. The typical structures of the BCN-Pt, CCN-Pt, 2CCN-Pt, 4CCN-Pt, CCN-Cy-Pt, and CCN-4Cy-Pt are shown in **Figure 5a-c** and **Fig. S3**.

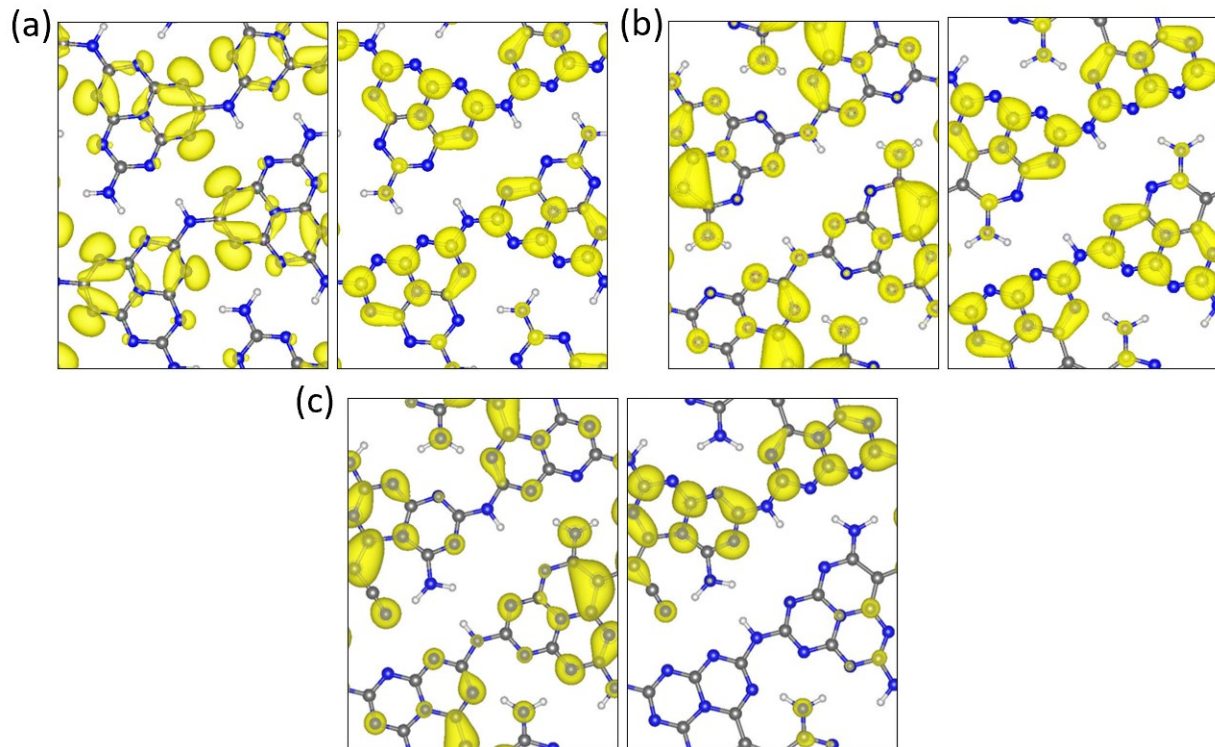


Fig. S2. Highest occupied molecular orbital (HOMO, left panel) and lowest unoccupied molecular orbital (LUMO, right panel) distribution of (a) C₂₄N₃₆H₁₂ (BCN), (b) C₂₈N₃₂H₁₂ (CCN), and (c) C₂₈N₃₂H₁₂-cyano (CCN-Cy). Reproduced from ¹. Copyright 2024, Royal Society of Chemistry.

Table S1. Effective masses of the electron (m_e) and hole (m_h) and the calculated reduced mass (μ) relative to the different crystal facets. Reproduced from ¹. Copyright 2024, Royal Society of Chemistry.

Samples	C/N	m_e	m_h	μ
C ₂₄ N ₃₆ H ₁₂ (BCN)	0.667	0.57 m_0	-1.79 m_0	0.43 m_0
C ₂₈ N ₃₂ H ₁₂ (CCN)	0.875	0.41 m_0	-2.17 m_0	0.35 m_0
C ₃₀ N ₃₀ H ₁₂ (2CCN)	1.000	1.43 m_0	-3.85 m_0	1.04 m_0
C ₃₂ N ₂₈ H ₁₂ (4CCN)	1.143	1.52 m_0	-4.55 m_0	1.14 m_0
C ₂₈ N ₃₂ H ₁₂ -cyano (CCN-Cy)	0.875	0.83 m_0	-2.94 m_0	0.66 m_0
C ₂₈ N ₃₂ H ₁₂ -4cyano (CCN-4Cy)	0.875	1.14 m_0	-10 m_0	1.02 m_0

μ represents reduced mass, $\mu = \left(1/m_e + 1/|m_h|\right)^{-1}$. m_0 is the free electron mass.

Table S2. H₂O adsorption energy (E_{H_2O}) and H* adsorption energy (E_H) in the ground state (GS) and excited state (ES).

Samples	E_{H_2O} (eV)		E_H (eV)	
	GS	ES	GS	ES
BCN-Pt	-0.69	-0.59	-0.64	-0.84
CCN-Pt	-0.61	-0.59	-0.01	-0.07
2CCN-Pt	-0.65	-0.61	-0.53	-0.26
4CCN-Pt	-0.64	-0.59	-0.03	-0.08
CCN-Cy-Pt	-0.74	-0.66	-0.66	-0.31
CCN-4Cy-Pt	-0.61	-0.57	-0.51	-0.25

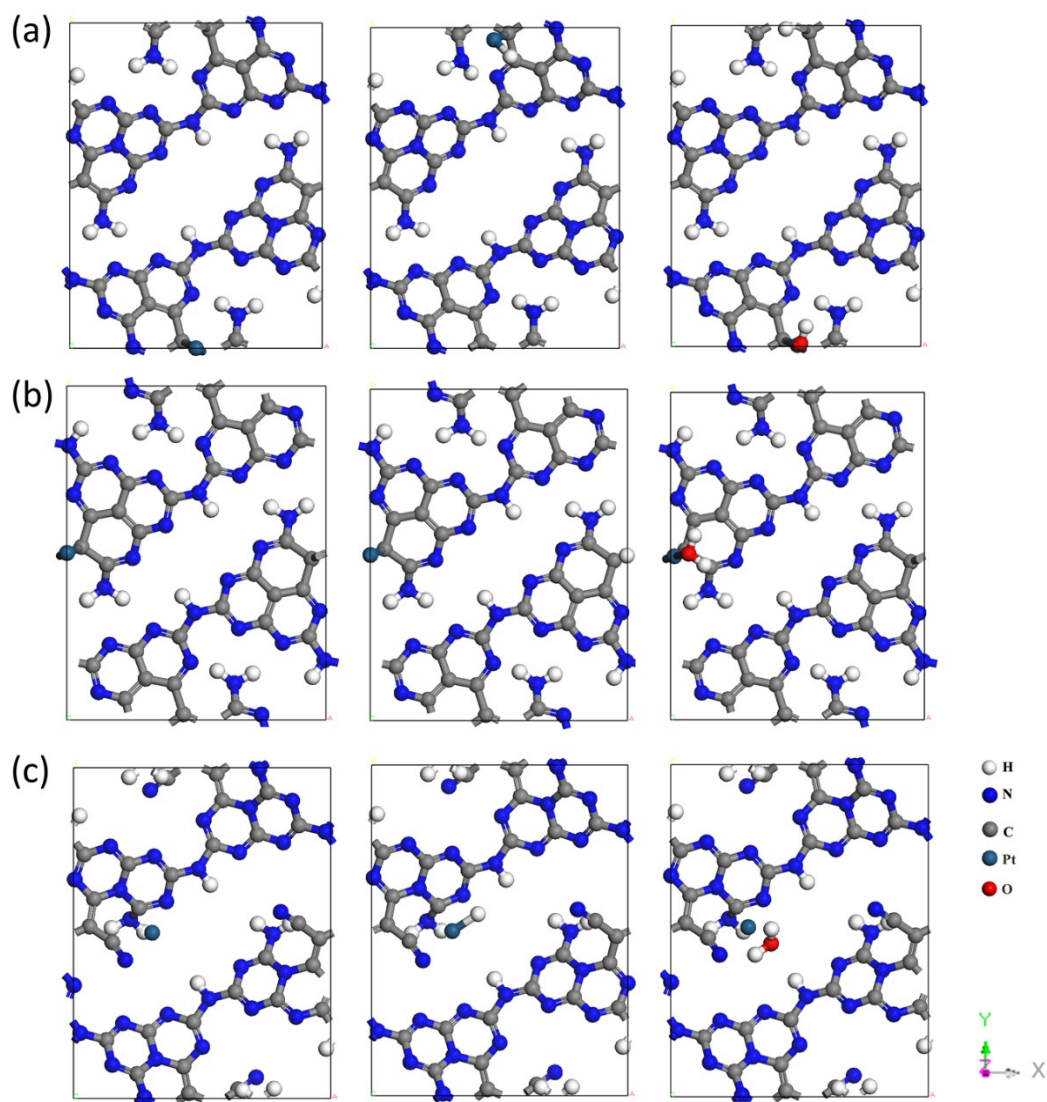


Fig. S3. DFT determined structure model of (left to right panels) Pt-loaded, H-adsorbed (Pt-loaded), and H₂O-adsorbed (Pt-loaded) (a) 2CCN, (b) 4CCN, and (c) CCN-4Cy. Pristine structure models reproduced from ¹. Copyright 2024, Royal Society of Chemistry.

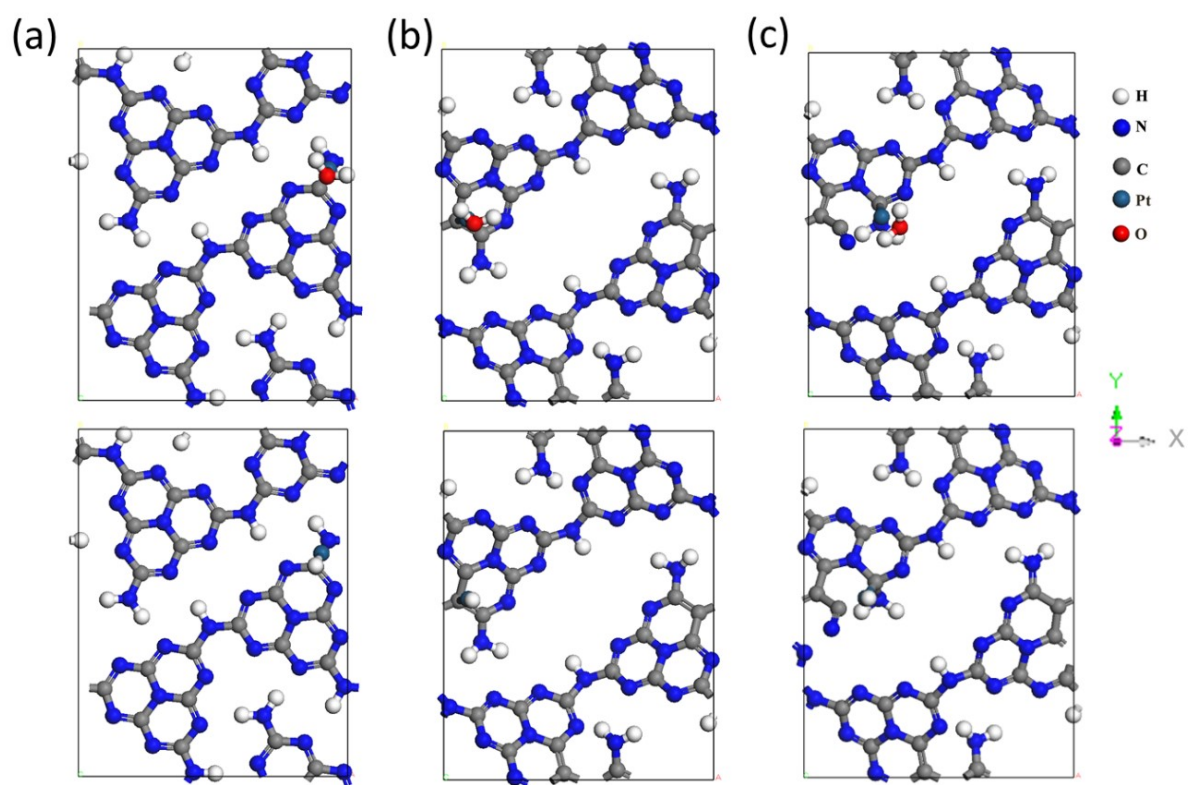


Fig. S4. DFT structure model of H₂O-adsorbed (top panels) and H-adsorbed (bottom panels) on (a) BCN-Pt, (b) CCN-Pt, and (c) CCN-Cy-Pt.

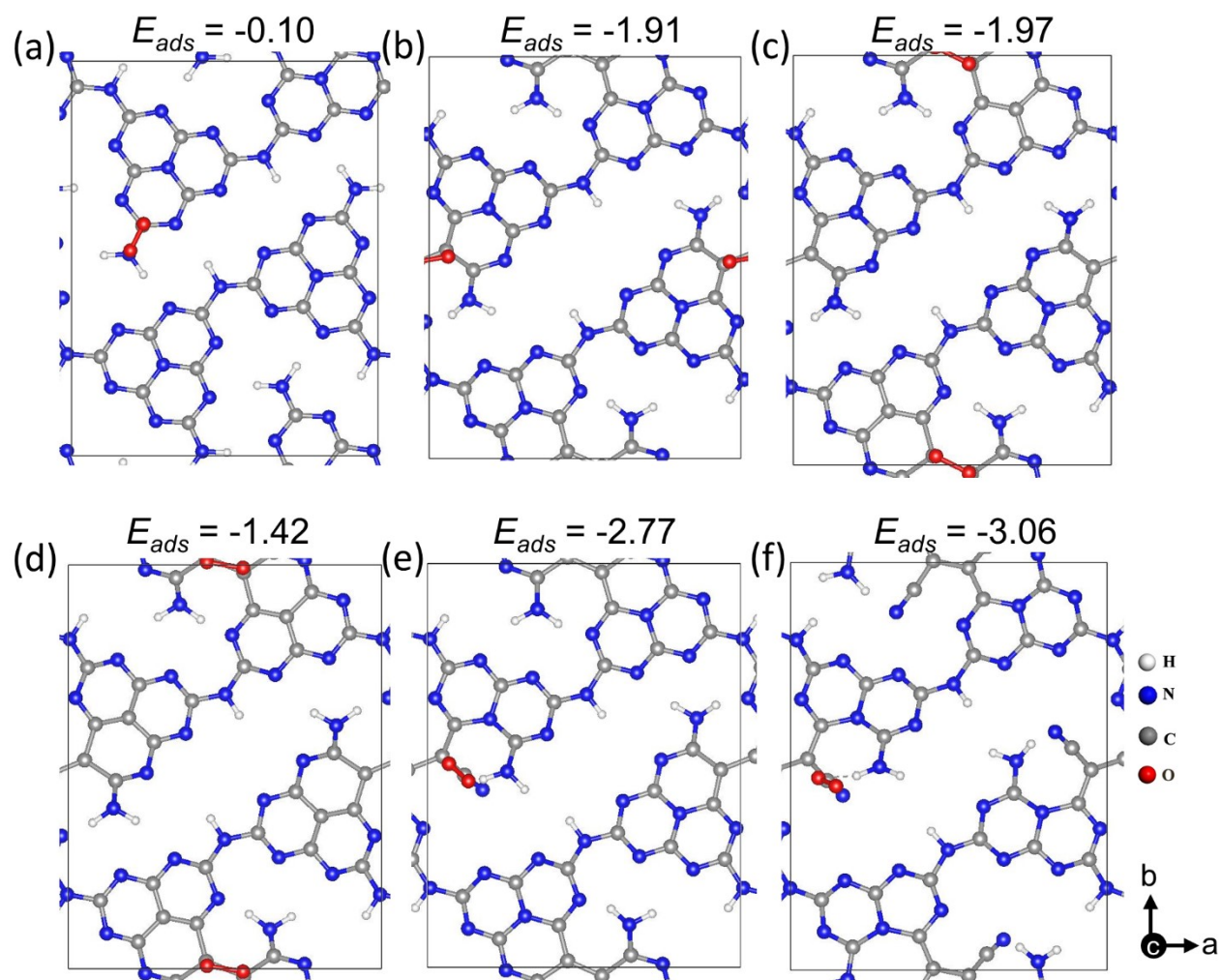


Fig. S5. Top view of the structure with O_2 adsorption on (a) BCN, (b) CCN, (c) 2CCN, (d) 4CCN, (e) CCN-Cy, and (f) CCN-4Cy.

Table S3. C and N p-band centres (ϵ_{Cp} and ϵ_{Np}) relative to the Fermi level (eV).

Samples	ϵ_{Cp}	ϵ_{Np}	$\Delta\epsilon_p = \epsilon_{Np} - \epsilon_{Cp}$
BCN	-6.47	-5.28	1.19
CCN	-6.73	-6.06	0.67
2CCN	-5.77	-5.09	0.68
4CCN	-5.25	-4.63	0.62
CCN-Cy	-6.74	-6.01	0.73
CCN-4Cy	-7.00	-6.25	0.75

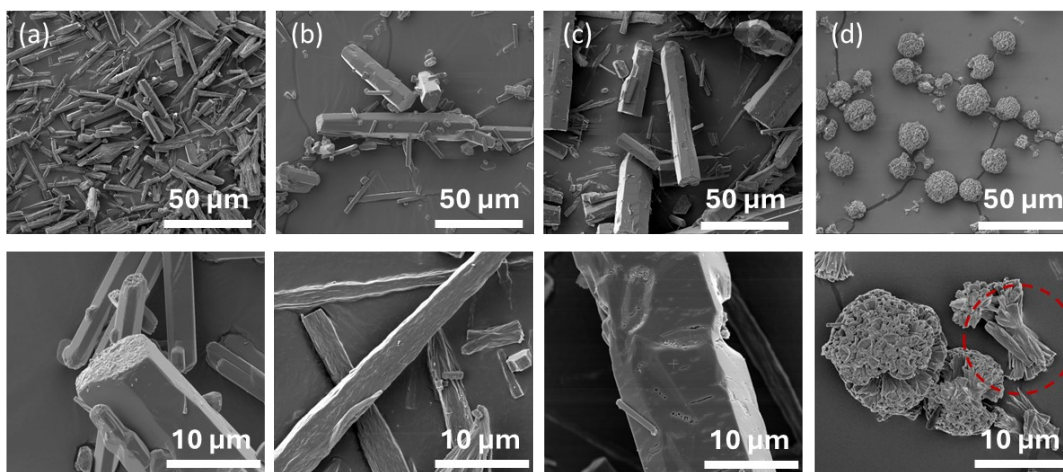


Fig. S6. SEM (top – low and bottom – high magnification) images of (a) melem hydrate and supramolecular precursors of (b) BCN, (c) CCN, and (d) of CCN-Cy.

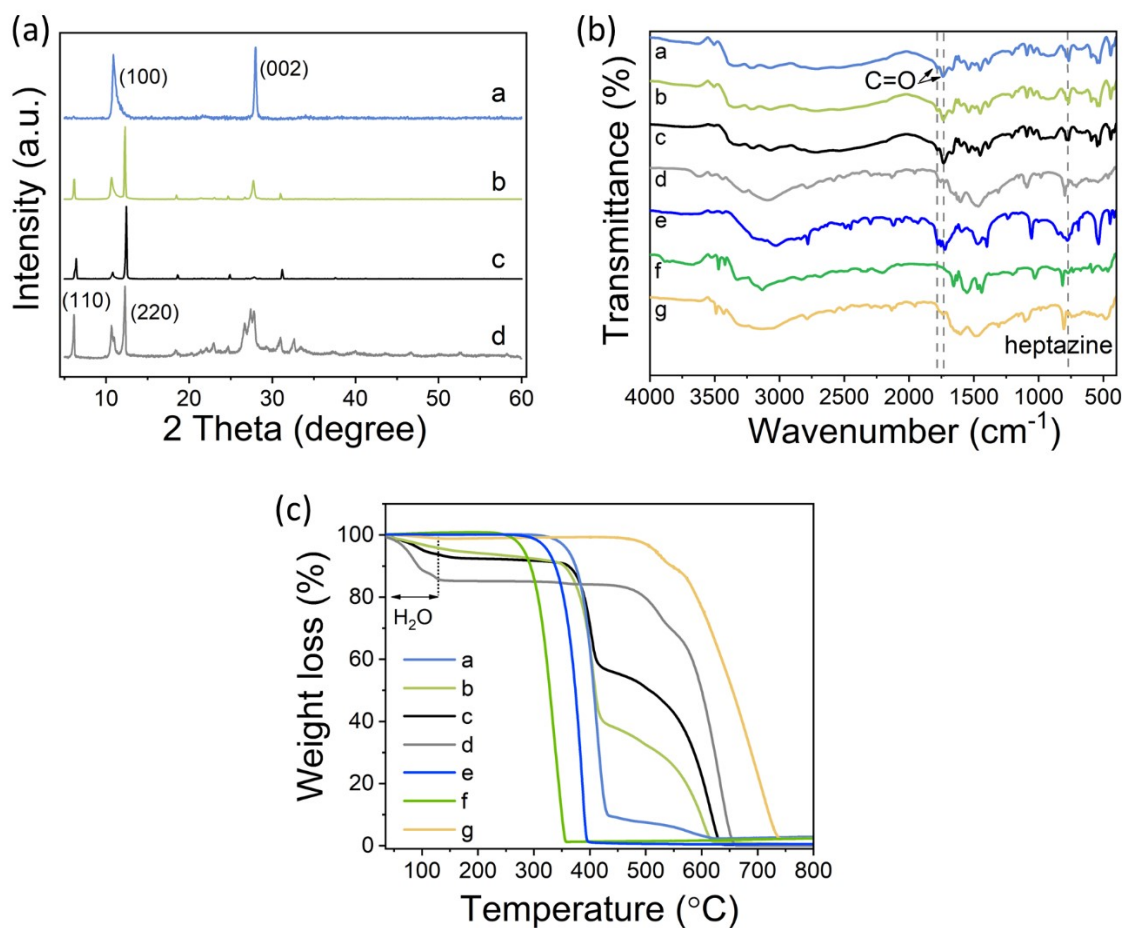


Fig. S7. (a) XRD patterns of melem hydrate and supramolecular precursors of a: CCN-Cy, b: CCN, c: BCN, and d: melem hydrate. (b) FTIR spectra and (c) TGA curves of supramolecular precursors of a: CCN-Cy, b: CCN, c: BCN, d: melem hydrate, e: cyanuric acid, f: melamine, and g: melem.

Table S4. C/N atomic ratio for BCN, CCN, 2CCN, 4CCN, CCN-Cy and CCN-4Cy obtained from XPS and EDS.

Sample	Calculated C/N atomic ratio	C/N atomic ratio from XPS	C/N atomic ratio from EDS
BCN	0.667	0.69	0.70
CCN	0.875	0.85	0.87
2CCN	1.000	0.97	0.95
4CCN	1.143	1.05	1.18
CCN-Cy	0.875	0.87	0.89
CCN-4Cy	0.875	0.86	0.88

Table S5. Surface properties of BCN, CCN, and CCN-Cy.

Sample	BET surface area (m²·g⁻¹)^a	Pore volume (cm³·g⁻¹)^b	Pore size (nm)^c
BCN	10.3	0.05	13.4
CCN	20.0	0.09	13.5
CCN-Cy	95.2	0.30	14.2

a) Specific surface area obtained by BET method, b) single point adsorption total pore volume at P/P₀ = 0.983 based on the BJH adsorption branch model, and c) peak of the pore size distribution.

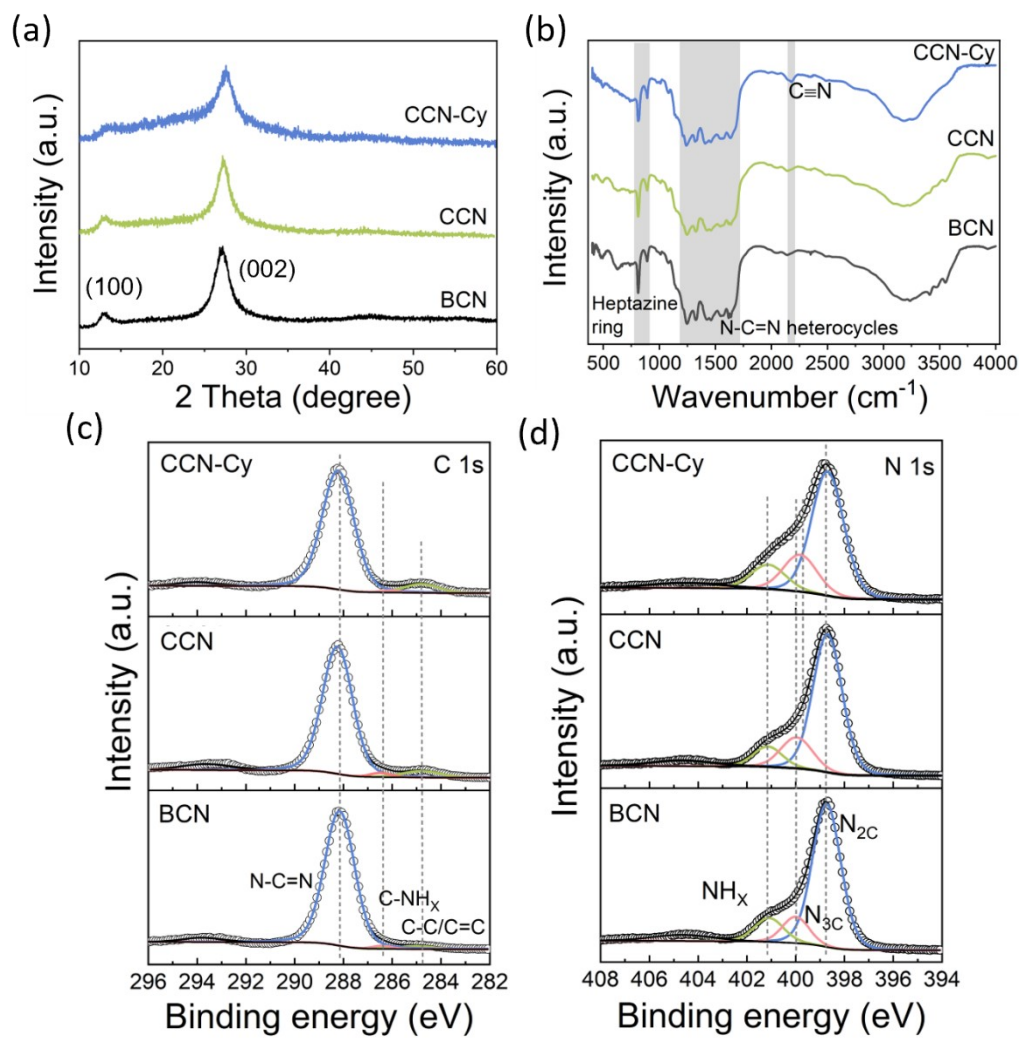


Fig. S8. (a) XRD patterns, (b) FTIR spectra, and high-resolution (c) C 1s and (d) N 1s XPS spectra of BCN, CCN, and CCN-Cy.

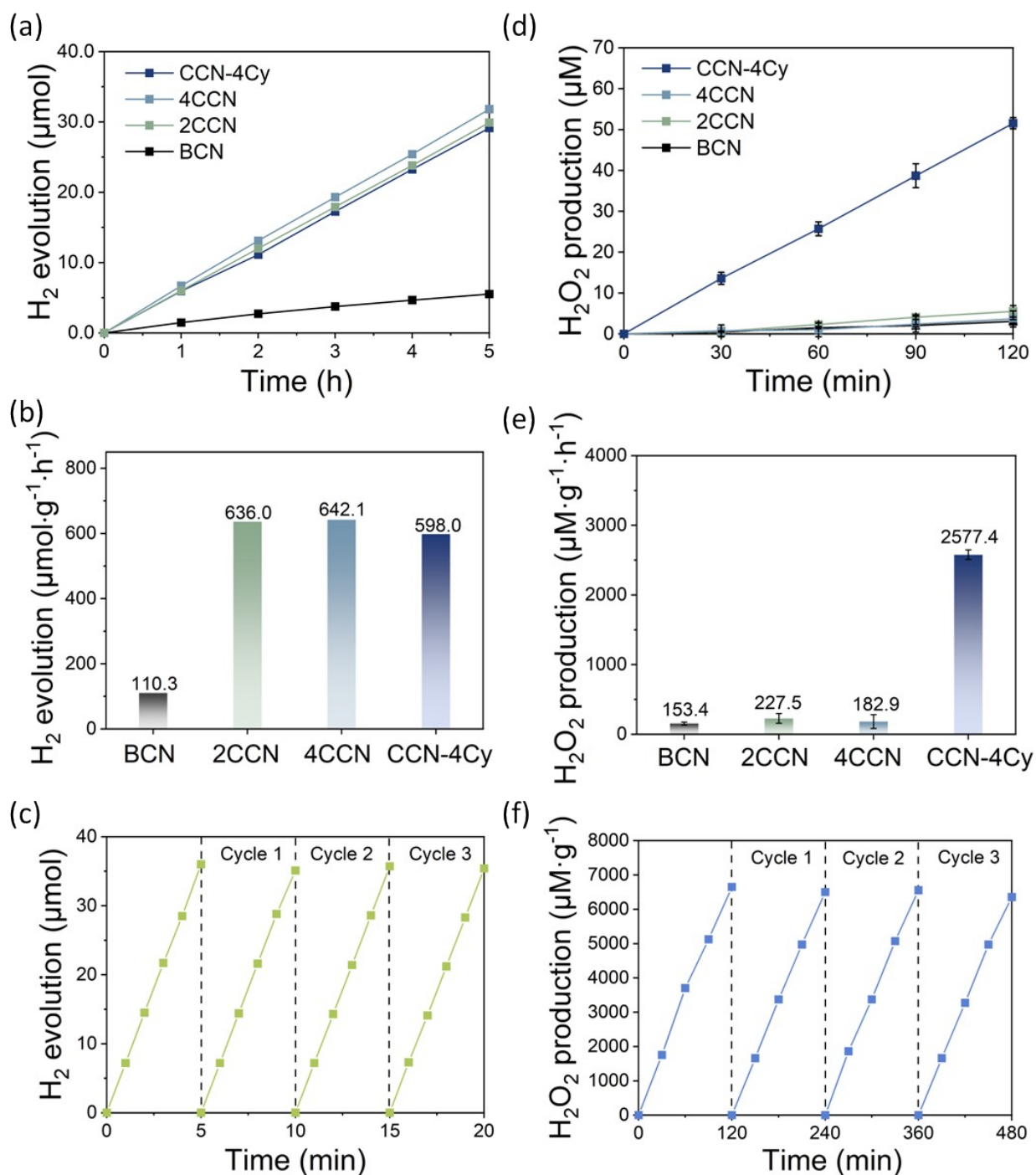


Fig. S9. (a) Hydrogen evolution with time and (b) hydrogen evolution rate of BCN, 2CCN, 4CCN, and CCN-4Cy. Conditions: 100 mL 10 vol.% methanol, 2 wt.% Pt, 10 mg catalyst, 5 h visible light irradiation ($\lambda > 420$ nm). (c) Recycled hydrogen evolution over CCN a further three times. (d) and (e) Photocatalytic H₂O₂ generation over BCN, 2CCN, 4CCN and CCN-4Cy. Conditions: 50 mL 10 vol.% ethanol, 10 mg catalyst, 2 h visible light irradiation ($\lambda > 420$ nm). (f) Recycling of CCN-4Cy for H₂O₂ production a further three times.

Table S6. H₂ generation rate and rate constant for the photodegradation of TC-HCl over BCN and CN-engineered CN samples.

Sample	H₂ evolution rate (μmol·g⁻¹·h⁻¹)	H₂O₂ generation (μM·g⁻¹·h⁻¹)
BCN	110.3	153.4
CCN	734.3	257.5
2CCN	636.0	227.5
4CCN	642.1	182.9
CCN-Cy	582.8	3702.1
CCN-4Cy	598.0	2577.4

Table S7. Hydrogen evolution performance over CN based photocatalysts reported in the literature.

Photocatalyst	Light source	Photocatalyst loading	Cocatalyst	Reaction solutions	H ₂ evolution rate ($\mu\text{mol}\cdot\text{g}^{-1}\cdot\text{h}^{-1}$)	Ref.
WO ₃ /TiO ₂ /rGO	350 W Xe lamp	0.50 g·L ⁻¹	-	20 vol.% methanol	245.8	17
CN/rGO/PDIP	300 W Xe lamp ($\lambda > 420$ nm)	0.25 g·L ⁻¹	Pt, Co(OH) ₂	10 vol.% TEOA	632	18
B-doped CN/ZnO	300 W Xe lamp	0.87 g·L ⁻¹	2 wt.% Pt	13 vol.% TEOA	357	19
Porous O-doped g-C ₃ N ₄ with N vacancies	300 W Xe lamp ($\lambda > 420$ nm)	1.00 g·L ⁻¹	3 wt.% Pt	10 vol.% TEOA	258.18	20
CN with cyano group and carbonyl group	300 W Xe lamp ($\lambda > 420$ nm)	1.00 g·L ⁻¹	3 wt.% Pt	10 vol.% TEOA	661	21
CN with N defects	300 W Xe lamp ($\lambda > 420$ nm)	0.21 g·L ⁻¹	3 wt.% Pt	12.5 vol.% TEOA	1882	22
P-doped CN nanotubes	300 W Xe lamp ($\lambda > 420$ nm)	1.00 g·L ⁻¹	3 wt.% Pt	10 vol.% TEOA	145.8	23
Ultra-thin CN nanosheets	300 W Xe lamp ($\lambda > 420$ nm)	0.60 g·L ⁻¹	3 wt.% Pt	10 vol.% TEOA	1254.7	24
Tubular CN with N defects and B doping	300 W Xe lamp ($\lambda > 420$ nm)	1.00 g·L ⁻¹	3 wt.% Pt	10 vol.% TEOA	789.2	25
C-doped CN	300 W Xe lamp ($\lambda > 420$ nm)	0.10 g·L ⁻¹	2 wt.% Pt	10 vol.% methanol	734.3	This work

rGO: reduced graphene oxide; PDIP: perylene diimide polymer; TEOA: triethanolamine.

Table S8. H₂O₂ production over CN based photocatalysts reported in the literature.

Photocatalyst	Light source	Reaction atmosphere	Reaction solution	Photocatalyst loading	H ₂ O ₂ yield (μM·g ⁻¹ ·h ⁻¹)	Ref.
P-doped CN	9 W blue LED lamp (410 < λ < 530 nm)	O ₂ bubbling	10 vol.% ethanol	0.5 g·L ⁻¹	1902.2	26
B-doped CN	6*20 W neon lamps	O ₂ bubbling	5 vol.% isopropanol	1.0 g·L ⁻¹	4240.3	27
C-doped CN	300 W Xe lamp (λ > 420 nm)	O ₂ bubbling	10 ppm	1.0 g·L ⁻¹	748.8	28
CN nanoplates	400 nm ≤ λ ≤ 700 nm	Air bubbling	10 vol.% isopropanol	1.0 g·L ⁻¹	1435.7	29
CN with N defects	300 W Xe lamp (λ > 420 nm)	O ₂ bubbling	10 vol.% isopropanol	1.0 g·L ⁻¹	4760	30
Carbon vacancy and cyano group modified CN	AM 1.5G light	Air	Water	2.0 g·L ⁻¹	4308.7	31
B-doped and cyano group modified CN	300 W Xe lamp (λ > 420 nm)	O ₂ bubbling	10 vol.% isopropanol	0.5 g·L ⁻¹	574	32
3D spherical porous CN	500 W Xe lamp (λ > 420 nm)	Air bubbling	10 vol.% ethanol	0.1 g·L ⁻¹	3702.1	This work

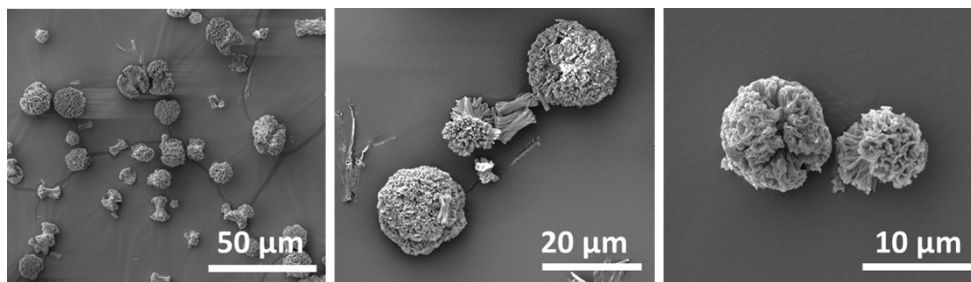


Fig. S10. SEM images at three magnifications of CCN-Cy after a total of four 2 h photodegradation reactions.

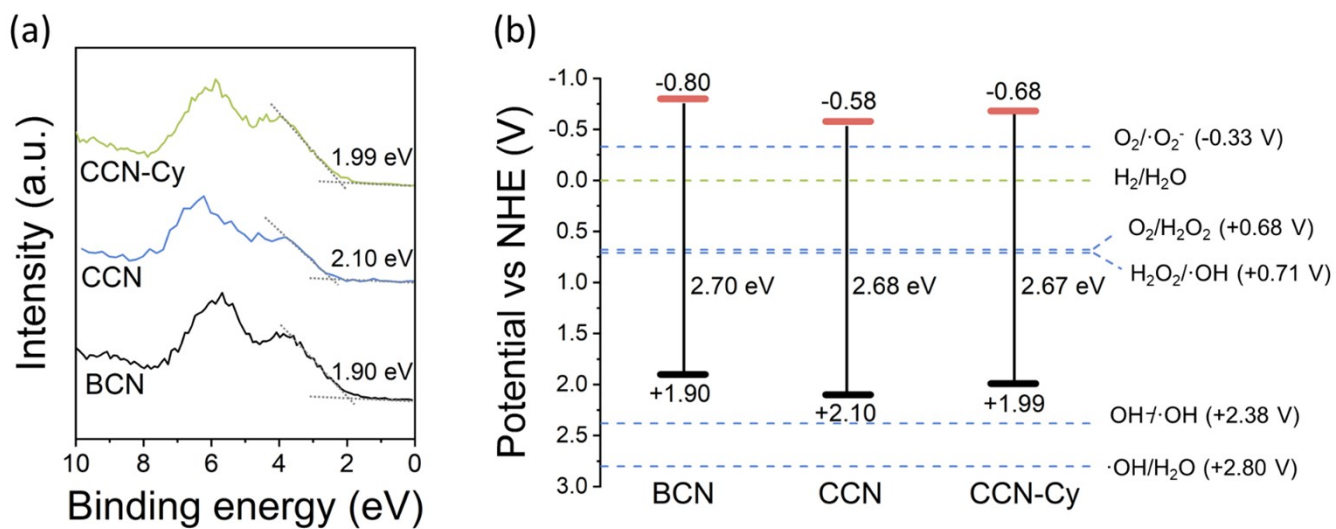


Fig. S11. (a) XPS VB spectra and (b) band structures of BCN, CCN, and CCN-Cy.

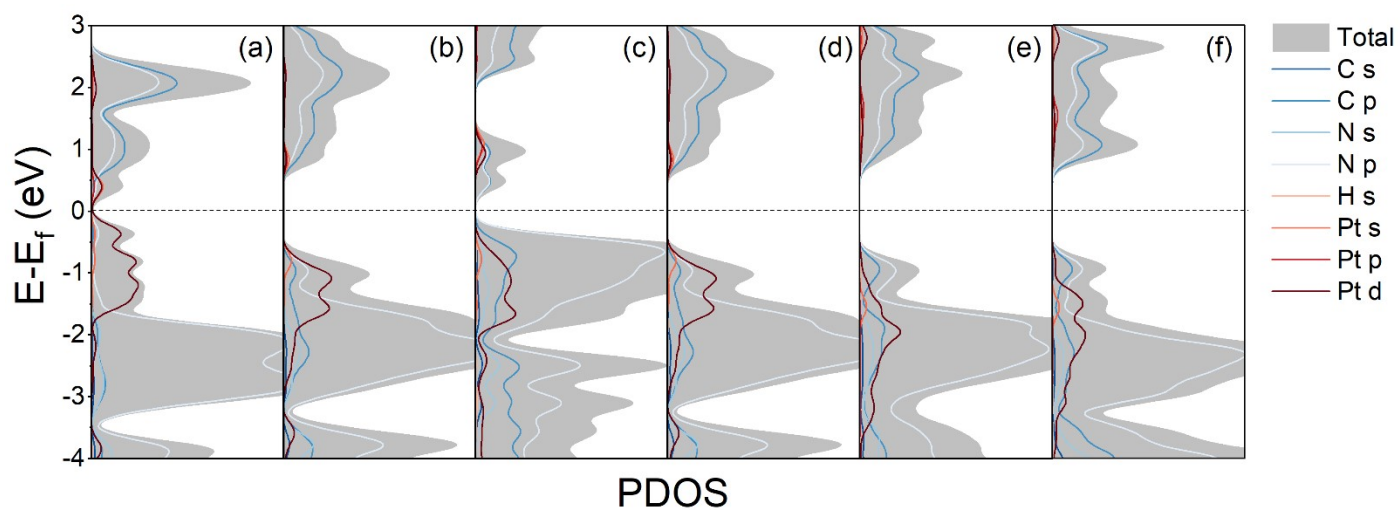


Fig. S12. PDOS for (a) BCN-Pt, (b) CCN-Pt, (c) 2CCN-Pt, (d) 4CCN-Pt, (e) CCN-Cy-Pt, and (f) CCN-4Cy-Pt.

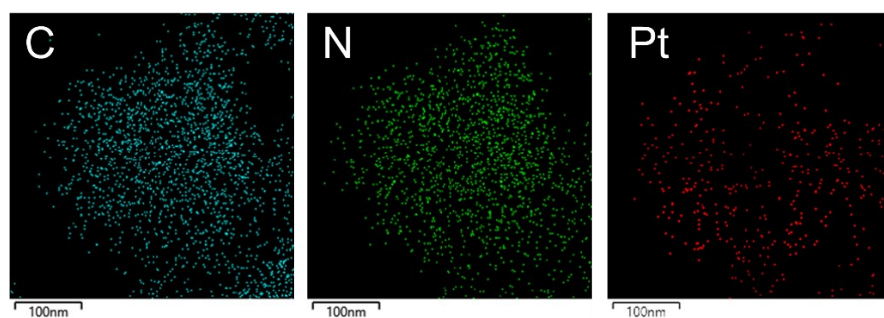


Fig. S13. Elemental mapping images of C, N, and Pt in CCN-Pt.

Table S9. ICP-MS data showing the Pt content of BCN-Pt, CCN-Pt, and CCN-Cy-Pt.

Sample	Pt (wt.%)
BCN-Pt	1.97
CCN-Pt	2.06
CCN-Cy-Pt	2.15

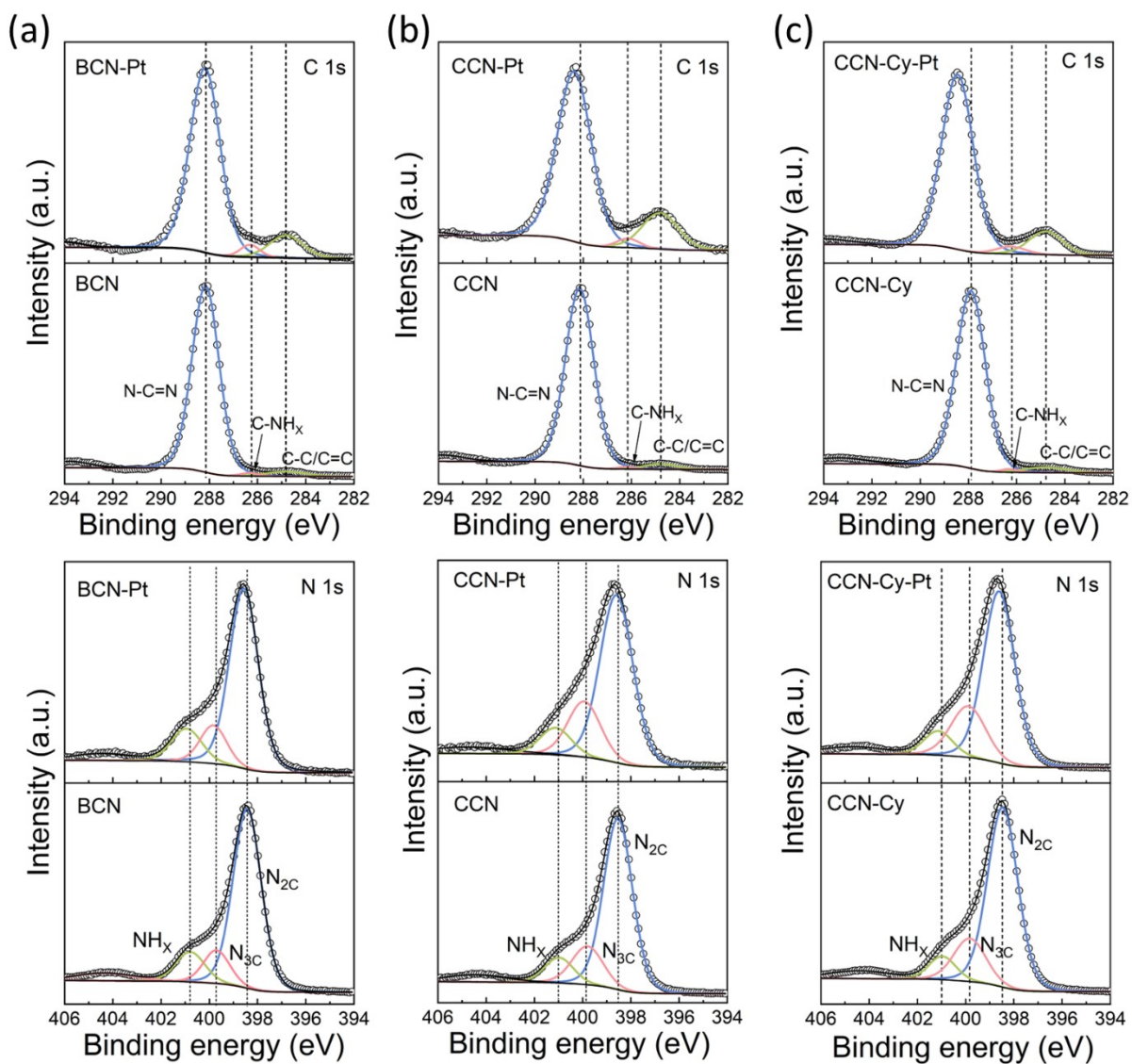


Fig. S14. C 1s (top panels) and N 1s (bottom panels) XPS spectra of (a) BCN and BCN-Pt, (b) CCN and CCN-Pt, and (c) CCN-Cy and CCN-Cy-Pt.

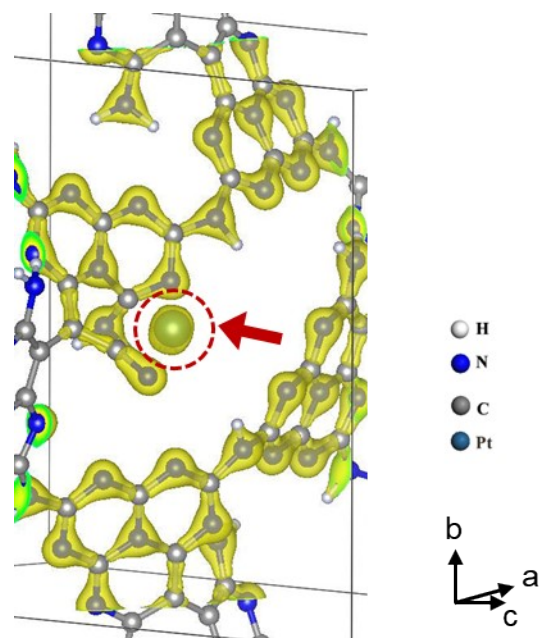


Fig. S15. Side view of 3D charge density difference of CCN-Cy-Pt with red arrow indicating the Pt atom encircled in red.

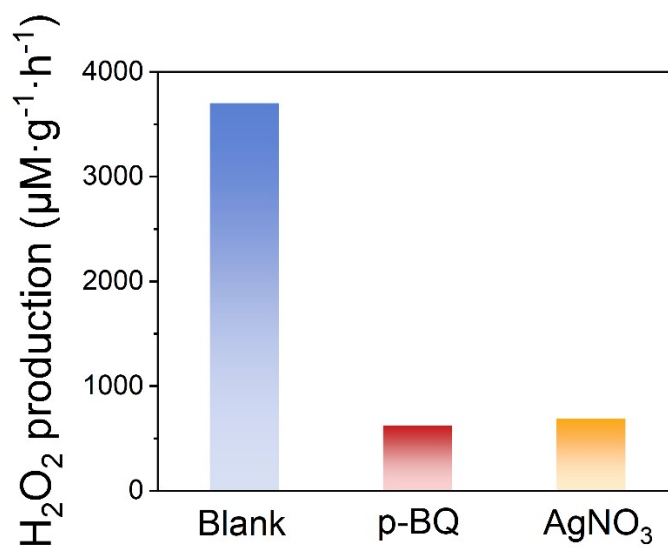


Fig. S16. Photocatalytic H_2O_2 generation with and without (Blank) radical scavengers (p-BQ and AgNO_3) over CCN-Cy.

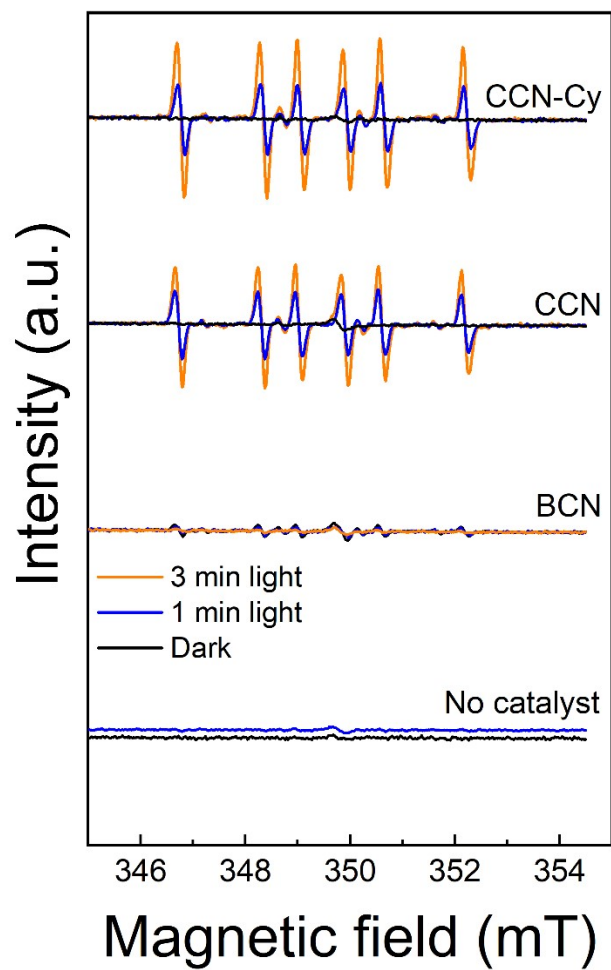


Fig. S17. *In-situ* EPR spectra of DMPO adducts measured without (no catalyst) or with the presence of BCN, CCN, and CCN-Cy in the dark or under light irradiation.

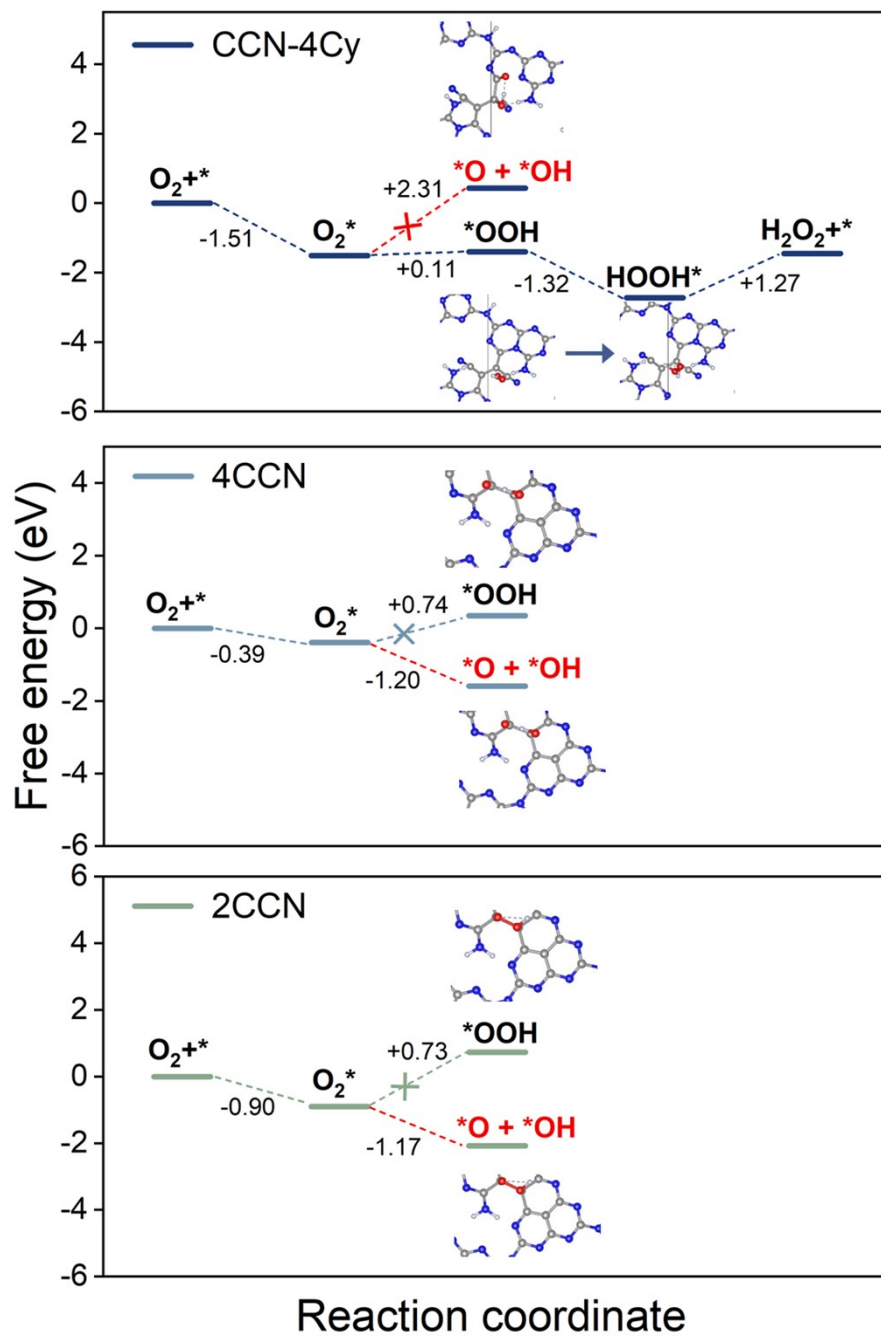


Fig. S18. Free energy profiles for photocatalytic H_2O_2 generation reactions over 2CCN, 4CCN, and CCN-4Cy.

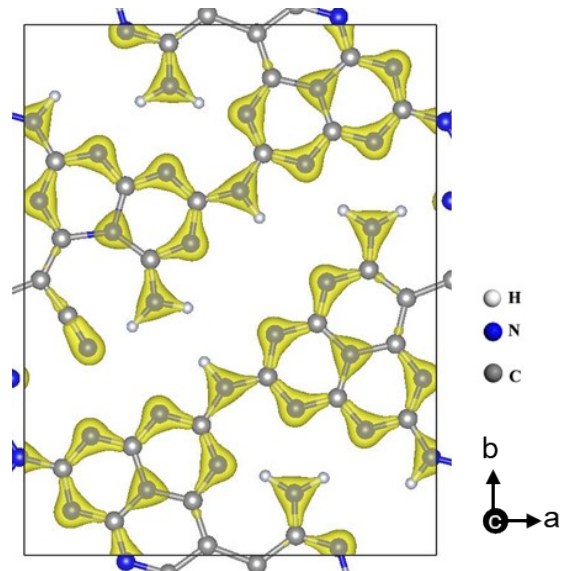


Fig. S19. Top view of 3D charge density difference of CCN-Cy.

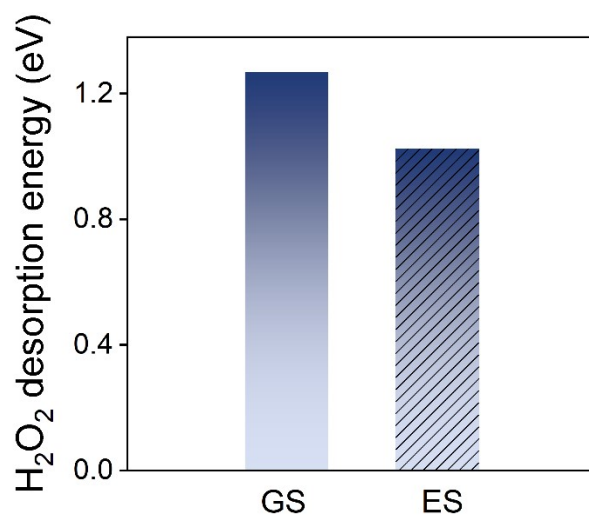


Fig. S20. H₂O₂ desorption energy in the GS and ES for CCN-4Cy.

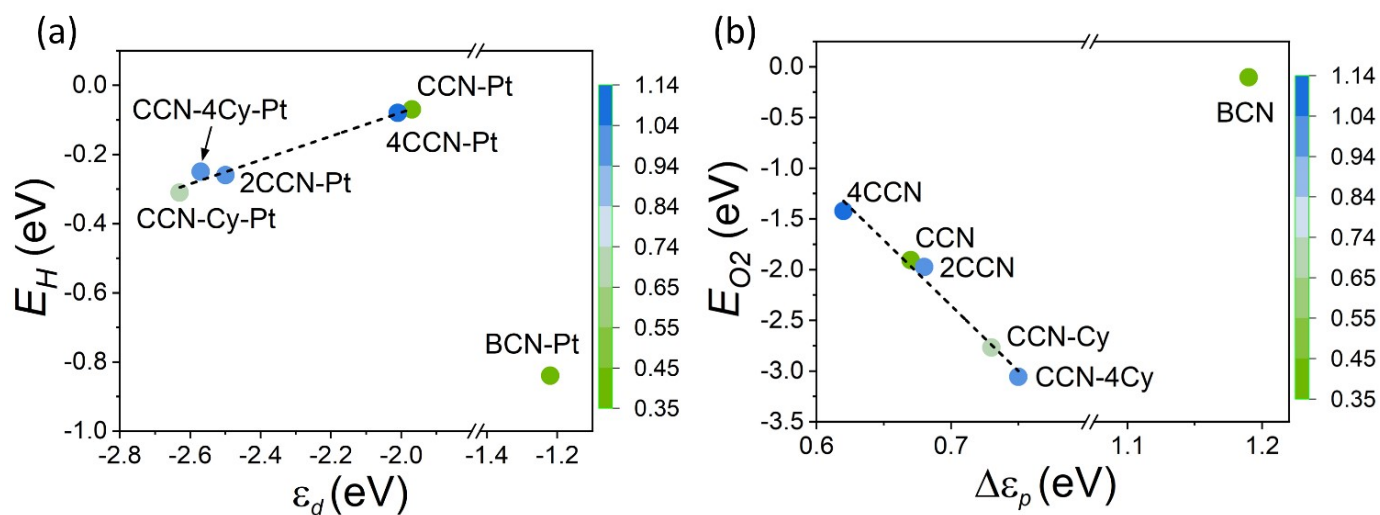


Fig. S21. (a) The adsorption energy of H^* (E_H) in the excited state (ES) for BCN-Pt and defect-engineered CN-Pt samples according to values of Pt d-band centres. (b) The adsorption energy of oxygen (E_{O_2}) in the ES for BCN and defect-engineered CN samples according to the $\Delta\epsilon_p$. The colour bars indicate the effective mass.

6. References

1. X. Li, H. Mai, X. Wang, Z. Xie, J. Lu, X. Wen, S. P. Russo, D. Chen and R. A. Caruso, *J. Mater. Chem. A.*, 2024, **12**, 5204-5214.
2. W. Kohn and L. J. Sham, *Phys. Rev.*, 1965, **140**, A1133-A1138.
3. P. Hohenberg and W. Kohn, *Phys. Rev.*, 1964, **136**, B864-B871.
4. G. Kresse and J. Furthmüller, *Phys. Rev. B: Condens. Matter Mater. Phys.*, 1996, **54**, 11169-11186.
5. G. Kresse and J. Furthmüller, *Comput. Mater. Sci.*, 1996, **6**, 15-50.
6. J. P. Perdew, K. Burke and M. Ernzerhof, *Phys. Rev. Lett.*, 1996, **77**, 3865-3868.
7. P. E. Blöchl, *Phys. Rev. B: Condens. Matter Mater. Phys.*, 1994, **50**, 17953-17979.
8. G. Kresse and D. Joubert, *Phys. Rev. B: Condens. Matter Mater. Phys.*, 1999, **59**, 1758-1775.
9. V. Wang, G. Tang, Y.-C. Liu, R.-T. Wang, H. Mizuseki, Y. Kawazoe, J. Nara and W. T. Geng, *J. Phys. Chem. Lett.*, 2022, **13**, 11581-11594.
10. Y. Zhu, C. Lv, Z. Yin, J. Ren, X. Yang, C.-L. Dong, H. Liu, R. Cai, Y.-C. Huang, W. Theis, S. Shen and D. Yang, *Angew. Chem. Int. Ed.*, 2020, **59**, 868-873.
11. R. Lin, J. Wan, Y. Xiong, K. Wu, W.-c. Cheong, G. Zhou, D. Wang, Q. Peng, C. Chen and Y. Li, *J. Am. Chem. Soc.*, 2018, **140**, 9078-9082.
12. J. Shen, C. Luo, S. Qiao, Y. Chen, Y. Tang, J. Xu, K. Fu, D. Yuan, H. Tang, H. Zhang and C. Liu, *ACS Catal.*, 2023, **13**, 6280-6288.
13. R. Garcia-Diaz, M. T. Romero de la Cruz, R. Ochoa Valiente, J. Guerrero-Sanchez and G. Hernández Cocolletzi, *Appl. Surf. Sci.*, 2019, **487**, 1394-1402.
14. C. Wu, S. Xue, Z. Qin, M. Nazari, G. Yang, S. Yue, T. Tong, H. Ghasemi, F. C. R. Hernandez, S. Xue, D. Zhang, H. Wang, Z. M. Wang, S. Pu and J. Bao, *Appl. Catal., B*, 2021, **282**.
15. D. Q. Dao, T. K. Anh Nguyen, S. G. Kang and E. W. Shin, *ACS Sustainable Chem. Eng.*, 2021, **9**, 14537-14549.
16. I. V. Solovyev, P. H. Dederichs and V. I. Anisimov, *Phys. Rev. B: Condens. Matter Mater. Phys.*, 1994, **50**, 16861-16871.
17. F. He, A. Meng, B. Cheng, W. Ho and J. Yu, *Chin. J. Catal.*, 2020, **41**, 9-20.
18. X. Chen, J. Wang, Y. Chai, Z. Zhang and Y. Zhu, *Adv. Mater.*, 2021, **33**, 2007479.
19. D. Kim and K. Yong, *Appl. Catal., B*, 2021, **282**, 119538.
20. Y. Jiang, Z. Sun, C. Tang, Y. Zhou, L. Zeng and L. Huang, *Appl. Catal., B*, 2019, **240**, 30-38.
21. J. Yang, Y. Liang, K. Li, G. Yang, K. Wang, R. Xu and X. Xie, *Appl. Catal., B*, 2020, **262**.
22. T. Yu, T. Xie, W. Zhou, Y. Zhang, Y. Chen, B. Shao, W.-Q. Guo and X. Tan, *ACS Sustainable Chem. Eng.*, 2021, **9**, 7529-7540.
23. D. Jang, S. Lee, N. H. Kwon, T. Kim, S. Park, K. Y. Jang, E. Yoon, S. Choi, J. Han, T.-W. Lee, J. Kim, S.-J. Hwang and S. Park, *Carbon*, 2023, **208**, 290-302.
24. L. Chen, X. Liang, H. Wang, Q. Xiao and X. Qiu, *Chem. Eng. J.*, 2022, **442**, 136115.
25. L. Chen, Y. Wang, S. Cheng, X. Zhao, J. Zhang, Z. Ao, C. Zhao, B. Li, S. Wang, S. Wang and H. Sun, *Appl. Catal., B*, 2022, **303**, 120932.
26. Z. Huang, F.-W. Yan and G.-q. Yuan, *ACS Sustainable Chem. Eng.*, 2018, **6**, 3187-3195.
27. Y. Ding, S. Maitra, C. Wang, R. Zheng, M. Zhang, T. Barakat, S. Roy, J. Liu, Y. Li, T. Hasan and B.-L. Su, *J. Energy Chem.*, 2022, **70**, 236-247.
28. T. Li, X. Zhang, C. Hu, X. Li, P. Zhang and Z. Chen, *J. Environ. Chem. Eng.*, 2022, **10**, 107116.
29. W. Liu, C. Song, M. Kou, Y. Wang, Y. Deng, T. Shimada and L. Ye, *Chem. Eng. J.*, 2021, **425**, 130615.
30. J. Luo, Y. Liu, C. Fan, L. Tang, S. Yang, M. Liu, M. Wang, C. Feng, X. Ouyang, L. Wang, L. Xu, J. Wang and M. Yan, *ACS Catal.*, 2021, **11**, 11440-11450.
31. S. Yan, Y. Li, X. Yang, X. Jia, J. Xu and H. Song, *Adv. Mater.*, 2024, **36**, 2307967.
32. C. Feng, L. Tang, Y. Deng, J. Wang, J. Luo, Y. Liu, X. Ouyang, H. Yang, J. Yu and J. Wang, *Adv. Funct. Mater.*, 2020, **30**, 2001922.